Entanglement-assisted detection of fading targets via correlation-to-displacement conversion

Xin Chen[1] and Quntao Zhuang[2,3,1,4,*]

[1]*Department of Electrical and Computer Engineering, University of Arizona, Tucson, Arizona 85721, USA*
[2]*Ming Hsieh Department of Electrical and Computer Engineering, University of Southern California, Los Angeles, California 90089, USA*
[3]*Department of Physics and Astronomy, University of Southern California, Los Angeles, California 90089, USA*
[4]*James C. Wyant College of Optical Sciences, University of Arizona, Tucson, Arizona 85721, USA*

(Received 3 January 2023; accepted 12 May 2023; published 5 June 2023)

Quantum illumination utilizes an entanglement-enhanced sensing system to outperform classical illumination in detecting a suspected target, despite the entanglement-breaking loss and noise. However, practical and optimal receiver design to fulfill the quantum advantage has been a long open problem. Recently, Shi *et al.* [arXiv:2207.06609 (2022)] proposed the correlation-to-displacement ('C→D') conversion module to enable an optimal receiver design that greatly reduces the complexity of the previous known optimal receiver [Q. Zhuang, Z. Zhang, and J. H. Shapiro, Phys. Rev. Lett. **118**, 040801 (2017)]. There, the analyses of the conversion module assume an ideal target with a known reflectivity and a fixed return phase. In practical applications, however, targets often induce a random return phase; moreover, their reflectivities can have fluctuations obeying a Rayleigh distribution. In this paper, we extend the analyses of the C→D module to realistic targets and show that the entanglement advantage is maintained albeit reduced. In particular, the conversion module allows exact and efficient performance evaluation despite the non-Gaussian nature of the quantum channel involved.

DOI: 10.1103/PhysRevA.107.062405

I. INTRODUCTION

Quantum entanglement enables performance boost in a wide range of optical sensing tasks, such as phase sensing [1,2], target detection and ranging [3–7], loss sensing [8–16], noise sensing [17,18], and gain sensing [19]. Despite the varieties of the applications, the sensing processes can often be modeled as bosonic Gaussian channels [20], which preserve the Gaussian form of input Wigner functions. The Gaussian nature of the quantum channel enables efficient exact evaluation of the sensing precision, especially when the source is also Gaussian [21,22]. Moreover, the structure of the Kraus operators of the bosonic Gaussian channel also allows the proof that Gaussian probes are optimal among all possible input states [1,16,18,19,23].

Taking target detection as an example, the transceiver-to-receiver path in the presence of a distant target can be modeled as a Gaussian thermal-loss channel with low transmissivity; when the target is absent, the thermal-loss channel degrades to its zero transmissivity limit. In a quantum illumination (QI) protocol with the common Gaussian entangled source of a two-mode squeezed vacuum, the error probability performance limit can be obtained via the efficiently calculable quantum Chernoff bound (QCB) [21,24], which enables the surprising discovery of a 6-dB error exponent advantage over classical illumination (CI) despite loss and noise [4].

Things become challenging when non-Gaussian elements are inevitably involved. To begin with, although the channel and source are Gaussian, receivers based on only Gaussian operations (e.g., optical-parametric amplification and phase conjugation) are only able to achieve half of the theoretical maximal 6-dB error exponent advantage [25]. Previously proposed optimal receiver design relies on complex non-Gaussian operations that forbid exact performance evaluations [5,26]. Moreover, a practical target detection scenario involves fading targets, where the random-phase noise and fluctuating reflectivity make the quantum channel non-Gaussian. The non-Gaussian nature of the problem makes it difficult to evaluate entanglement's advantage in detecting fading targets.

In this paper, we utilize the recently proposed correlation-to-displacement ('C→D') conversion module [27] to evaluate entanglement's advantage in a practical QI target detection scenario with fading targets. The conversion module reduces multimode correlated state detection to single-mode coherent-state detection, enabling optimal receiver design and also efficient evaluation even when non-Gaussian elements are involved. Our results show that when there is only correlated phase noise across the probing, the error probability still decays exponentially with the number of probing. Entanglement's error-exponent advantage is still 6 dB when the signal brightness is extremely small, but degrades as the brightness increases. Such robustness resembles previous findings in the communication case [28]. In the presence of transmissivity fluctuation of the Rayleigh type, however, the error probability decays polynomially with the number of probes, and the advantage from entanglement is small, despite being nonzero.

II. MODEL FOR FADING TARGET DETECTION

As shown in Fig. 1, in an entanglement-assisted QI target detection scenario, the probe signal is entangled with an

*qzhuang@usc.edu

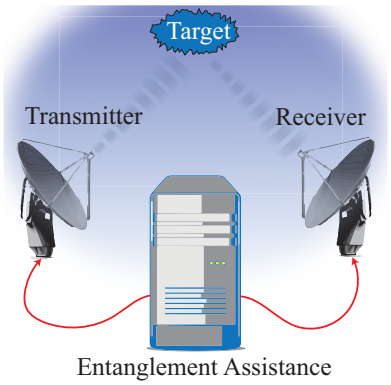

FIG. 1. Concept of entanglement-assisted target detection. The target surface can be rough, causing fading effects.

ancilla. The signal is reflected by a stationary target in a highly lossy and noisy environment before being detected. A properly structured receiver is required to measure the received signal and the ancilla to boost the sensing precision over CI. In the ideal case of a known phase and a fixed target reflectivity, this process can be modeled as an overall phase-shift thermal-loss channel $\Phi_{\kappa,\theta}$ [20], with κ being the transmissivity and θ being the phase shift (as shown in Fig. 2). For an input mode described by the annihilation operators $\hat{a}_{\rm S}$, the received mode is

$$\hat{a}_{\rm R} = e^{i\theta}\sqrt{\kappa}\hat{a}_{\rm S} + \sqrt{1-\kappa}\hat{a}_{\rm B}, \tag{1}$$

where the mode $\hat{a}_{\rm B}$ is in a thermal state with mean photon number $N_{\rm E}$ to model the noise.

To model a realistic setting, we consider a target with a time-independent $P_K(\cdot)$-distributed random reflectivity and $P_\Theta(\cdot)$-distributed random-phase shift. This leads to the overall quantum channel:

$$\bar{\Phi} = \int d\theta d\kappa P_\Theta(\theta) P_K(\kappa) \Phi_{\kappa,\theta}. \tag{2}$$

The target detection hypothesis testing problem is therefore a quantum channel discrimination problem between the channel $\bar{\Phi}$ (fading target present) and a pure noise channel $\Phi_{0,0}$.

To benefit from entanglement in QI, we consider M signal-idler pairs $\{\hat{a}_{S_m}, \hat{a}_{I_m}\}_{m=1}^M$, where each pair is in a two-mode squeezed-vacuum state with the wave function

$$\hat{\phi}_{S_m I_m} = \sum_{n=0}^{\infty} \sqrt{\frac{N_{\rm S}^n}{(N_{\rm S}+1)^{n+1}}} |n\rangle_{S_m} |n\rangle_{I_m}. \tag{3}$$

Here $|n\rangle$ is the number state and $N_{\rm S}$ is the mean photon number of the signal (or idler) mode.

When the target is present, after the channel $\bar{\Phi}$, the density operator of the return and idler field is

$$\hat{\rho}_{\rm RI} = \int d\theta d\kappa P_\Theta(\theta) P_K(\kappa) \hat{\rho}_{\rm RI}(\theta,\kappa). \tag{4}$$

Here the state $\hat{\rho}_{\rm RI}(\theta,\kappa)$ describes the M return-idler pairs $\{\hat{a}_{R_m}, \hat{a}_{I_m}\}_{m=1}^M$ from channel $\Phi_{\kappa,\theta}$, each maintaining a phase-sensitive cross-correlation $\langle \hat{a}_{R_m}\hat{a}_{I_m}\rangle = e^{i\theta}C_p$ with the amplitude $C_p \equiv \sqrt{\kappa N_{\rm S}(N_{\rm S}+1)}$.

III. ANALYSES OF THE CORRELATION-TO-DISPLACEMENT CONVERSION MODULE

As shown in Fig. 2, in a C→D conversion module [27], we perform heterodyne measurement on each return mode and retain the idlers for further information processing. In general, the measurement can be described by positive operator-valued measure (POVM) elements $\hat{E}_{\boldsymbol{x}}^\dagger \hat{E}_{\boldsymbol{x}}$ satisfying the completeness relation $\int d^{2M}\boldsymbol{x}\, \hat{E}_{\boldsymbol{x}}^\dagger \hat{E}_{\boldsymbol{x}} = \hat{I}$, where the overall measurement result across the M returns $\boldsymbol{x} = (x_1, \cdots, x_M)^T$ with each x_m being complex.

The corresponding probability of having measurement result $\boldsymbol{X} = \boldsymbol{x}$ is given by

$$P_{\boldsymbol{X}}(\boldsymbol{x}) = {\rm Tr}(\hat{\rho}_{\rm RI}\hat{E}_{\boldsymbol{x}}^\dagger \hat{E}_{\boldsymbol{x}}) \tag{5}$$

$$= \int d\theta d\kappa P_\Theta(\theta) P_K(\kappa) P_{\boldsymbol{X}|\Theta,K}(\boldsymbol{x}|\theta,\kappa), \tag{6}$$

with $P_{\boldsymbol{X}|\Theta,K}(\boldsymbol{x}|\theta,\kappa) = {\rm Tr}[\hat{\rho}_{\rm RI}(\theta,\kappa)\hat{E}_{\boldsymbol{x}}^\dagger \hat{E}_{\boldsymbol{x}}]$ as the conditional probability when the channel is $\Phi_{\kappa,\theta}$, where we have used Eq. (4). For a given fixed phase and reflectivity, the distribution has been solved in Ref. [27] as a complex Gaussian distribution with variance $2\sigma_\kappa^2 = \kappa N_{\rm S} + (1-\kappa)N_{\rm E} + 1$, i.e.,

$$P_{\boldsymbol{X}|\Theta,K}(\boldsymbol{x}|\theta,\kappa) = g(|\boldsymbol{x}|,\sigma_k), \tag{7}$$

where we define $g(x,\sigma) = e^{-x^2/2\sigma^2}/(2\pi\sigma^2)^M$. Note that $P_{\boldsymbol{X}|\Theta,K}(\boldsymbol{x}|\theta,\kappa)$ does not depend on the phase shift θ; therefore, we obtain the unconditional distribution of the measurement result as

$$P_{\boldsymbol{X}}(\boldsymbol{x}) = \int d\kappa P_{K,\boldsymbol{X}}(\kappa,\boldsymbol{x}), \tag{8}$$

with $P_{K,\boldsymbol{X}}(\kappa,\boldsymbol{x}) \equiv P_K(\kappa)P_{\boldsymbol{X}|\Theta,K}(\boldsymbol{x}|\theta,\kappa) = P_K(\kappa)g(|\boldsymbol{x}|,\sigma_k)$. At the same time, the conditional distribution can be obtained as

$$P_{K|\boldsymbol{X}}(\kappa|\boldsymbol{x}) = \frac{P_K(\kappa)g(|\boldsymbol{x}|,\sigma_k)}{\int d\kappa P_K(\kappa)g(|\boldsymbol{x}|,\sigma_k)} \equiv f(\kappa,|\boldsymbol{x}|), \tag{9}$$

which is only a function of the module $|\boldsymbol{x}|$ and κ.

Conditioned on the measurement result of the return mode, the signal return-idler joint state is

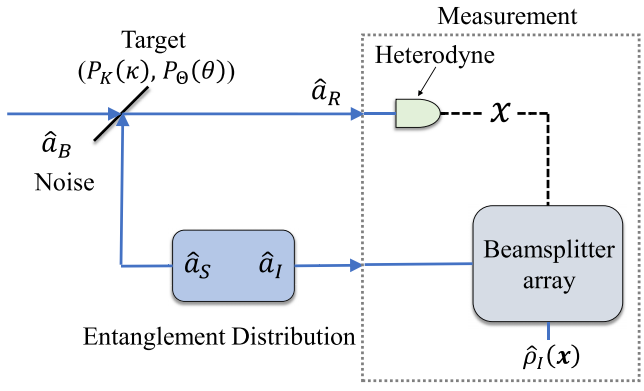

FIG. 2. Schematic illustration of the C→D conversion module.

projected to

$$\hat{\rho}'_{\rm RI}(\boldsymbol{x}) = \frac{\hat{E}_{\boldsymbol{x}}\hat{\rho}_{\rm RI}\hat{E}_{\boldsymbol{x}}^{\dagger}}{P_X(\boldsymbol{x})} \tag{10}$$

$$= \frac{\int d\theta d\kappa P_\Theta(\theta)P_K(\kappa)\hat{E}_{\boldsymbol{x}}\hat{\rho}_{\rm RI}(\theta,\kappa)\hat{E}_{\boldsymbol{x}}^{\dagger}}{P_X(\boldsymbol{x})} \tag{11}$$

$$= \int d\theta d\kappa \frac{P_\Theta(\theta)P_{K,X}(\kappa,\boldsymbol{x})}{P_X(\boldsymbol{x})}\hat{\rho}_{\rm RI}(\theta,\kappa|\boldsymbol{x}), \tag{12}$$

where the conditional state

$$\hat{\rho}_{\rm RI}(\theta,\kappa|\boldsymbol{x}) = \frac{\hat{E}_{\boldsymbol{x}}\hat{\rho}_{\rm RI}(\theta,\kappa)\hat{E}_{\boldsymbol{x}}^{\dagger}}{P_{X|\Theta,K}(\boldsymbol{x}|\theta,\kappa)} \tag{13}$$

is identical to the return-idler state after the heterodyne detection, from the Gaussian channel $\Phi_{\kappa,\theta}$ with fixed phase shift θ and reflectivity κ in Ref. [27]. The first line of Eq. (10) follows from definition of POVM; In the second line of Eq. (11), we have utilized Eq. (4). The last line of Eq. (12) comes from the fact that $P_{K,X}(\kappa,\boldsymbol{x}) \equiv P_K(\kappa)P_{X|\Theta,K}(\boldsymbol{x}|\theta,\kappa)$.According to Ref. [27], the idler mode of $\hat{\rho}_{\rm RI}(\theta,\kappa|\boldsymbol{x})$ is a product of the displaced thermal state:

$$\mathrm{Tr}_R[\hat{\rho}_{\rm RI}(\theta,\kappa|\boldsymbol{x})] = \otimes_m \hat{\rho}_{d_m,E_\kappa}. \tag{14}$$

The complex displacement of the idler conditioned on the measurement result is $d_m = \mu_\kappa e^{i\theta}\boldsymbol{x}_m^*$, with

$$\mu_\kappa = \frac{\sqrt{\kappa N_{\rm S}(N_{\rm S}+1)}}{[\kappa N_{\rm S} + (1-\kappa)N_{\rm E} + 1]}, \tag{15}$$

and the thermal noise mean photon number

$$E_\kappa = \frac{(1-\kappa)(1+N_{\rm E})N_{\rm S}}{[\kappa N_{\rm S} + (1-\kappa)N_{\rm E} + 1]}. \tag{16}$$

Conditioned on phase θ and reflectivity κ, one can apply the beamsplitter array strategy in Ref. [27] on the idler modes with the weights of the beamsplitter properly chosen based on the heterodyne detection result (independent of θ or κ), producing a one-mode displaced thermal state with the complex displacement, $d = \sum \omega_m d_m = \mu_\kappa e^{i\theta}|\boldsymbol{x}|$, where the weight $\omega_m = \boldsymbol{x}_m/|\boldsymbol{x}|$ is independent of κ, θ. The mean photon number of the displaced thermal state is still E_κ. Considering the phase shift and reflectivity distribution, the unconditional output state of the single output mode is

$$\hat{\rho}_{\rm I}(\boldsymbol{x}) = \int d\kappa P_{K|X}(\kappa|\boldsymbol{x})\hat{\rho}_{{\rm I},\kappa}(\boldsymbol{x}) \tag{17}$$

where the conditional state

$$\hat{\rho}_{{\rm I},\kappa}(\boldsymbol{x}) \equiv \int d\theta\, P_\Theta(\theta)\hat{\rho}_{\mu_\kappa e^{i\theta}|\boldsymbol{x}|,E_\kappa}. \tag{18}$$

Note that when the phase is uniform random in $[0, 2\pi)$, $\hat{\rho}_{{\rm I},\kappa}(\boldsymbol{x})$ is photon number diagonal (see Appendix A). Similar to Eq. (3) of Ref. [27], the error probability performance limit of QI based on the C→D conversion module is therefore

$$P_{\rm C\to D} = \int d^{2M}\boldsymbol{x} P_X(\boldsymbol{x})P_{\rm H}[\hat{\rho}_{0,N_{\rm S}}, \hat{\rho}_{\rm I}(\boldsymbol{x})], \tag{19}$$

where $P_{\rm H}(\hat{\rho},\hat{\sigma})$ is the Helstrom bound of the error probability in discriminating the states $\hat{\rho}$ and $\hat{\sigma}$ with equal prior probability [27,29–31].

Noticing that the state $\hat{\rho}_{\rm I}(\boldsymbol{x})$ and the distribution $P_X(\boldsymbol{x})$ are only functions of the amplitude $|\boldsymbol{x}|$ and making use of Eqs. (9) and (7) explicitly, we can further simplify the result via integrating out the $2M-1$ degree of freedom to obtain

$$P_{\rm C\to D} = \int dx P_X(x)P_{\rm H}[\hat{\rho}_{0,N_{\rm S}}, \hat{\rho}_{\rm I}(x)]. \tag{20}$$

Here

$$P_X(x) = \frac{2\pi^M}{\Gamma(M)}\int d\kappa P_K(\kappa)x^{2M-1}\, g(x,\sigma_k). \tag{21}$$

is the distribution of the module of measurement result $\boldsymbol{x}$, and the corresponding conditional state

$$\hat{\rho}_{\rm I}(x) = \int d\theta d\kappa P_\Theta(\theta)f(\kappa,x)\hat{\rho}_{\mu_\kappa e^{i\theta}x,E_\kappa}. \tag{22}$$

IV. PERFORMANCE FOR THE RANDOM-PHASE MODEL (KNOWN REFLECTIVITY)

A. Evaluating the performance of the conversion module

To understand the effect of phase noise, we begin with the scenario of uniformly distributed phase shift and a fixed known reflectivity κ. Therefore, the phase noise distribution $P_\Theta(\theta) = 1/2\pi$ and the reflectivity is a delta function, $P_K(\kappa') = \delta(\kappa'-\kappa)$. Consequently, $\hat{\rho}_{\rm I} = \hat{\rho}_{{\rm I},\kappa}$ in Eq. (17) is diagonal in the number basis regardless of the target's presence or absence. Therefore, photon counting is the optimal measurement and the error probability performance limit can be analytically solved from Eqs. (20) and (21):

$$P_{\rm C\to D} = \int dy_\kappa P_{\chi^2}^{(2M)}(y_\kappa)P_{\rm H}[\hat{\rho}_{0,N_{\rm S}}, \hat{\rho}_{{\rm I},\kappa}(\sigma_\kappa\sqrt{y_\kappa})] \tag{23}$$

where $P_{\chi^2}^{(2M)}(\cdot)$ is the χ^2 distribution of $2M$ degrees of freedom and we have changed the variable x to $y_\kappa = x^2/\sigma_\kappa^2$ from Eq. (20). At the same time, we can explicitly solve

$$P_{\rm H}[\hat{\rho}_{0,N_{\rm S}}, \hat{\rho}_{{\rm I},\kappa}(\sigma_\kappa\sqrt{y_\kappa})] = \left[1 - \sum_{n:\gamma_{n,\kappa}(y_k)>0}\gamma_{n,\kappa}(y_k)\right]\Big/2, \tag{24}$$

where we have defined (see Appendix A)

$$\gamma_{n,\kappa}(y_\kappa) = \frac{N_{\rm S}^n}{(1+N_{\rm S})^{n+1}} - \frac{E^n}{(1+E)^{1+n}}e^{-\xi_\kappa y_\kappa/E}\,{}_1\tilde{F}_1\left[n+1, 1, \frac{\xi_\kappa y_\kappa}{E(1+E)}\right], \tag{25}$$

and the summation includes all positive values of $\gamma_n(y)$. Here ${}_1\tilde{F}_1$ is the regularized confluent hypergeometric function [32] and

$$\xi_\kappa = \mu_\kappa^2\sigma_\kappa^2 = \frac{\kappa N_{\rm S}(N_{\rm S}+1)}{2[\kappa N_{\rm S} + (1-\kappa)N_{\rm E} + 1]}. \tag{26}$$

Moreover, by the central limit theorem, at the limit of $M \gg 1$, the χ^2 distribution $P_{\chi^2}^{(2M)}(y_\kappa)$ in Eq. (23) can be approximated as a Gaussian distribution with mean $2M$ and variance $4M$. Because the standard deviation $\sqrt{4M}$ is much smaller than the mean $2M$ when M is large, in our evaluation we can ignore the fluctuations and directly utilize $y_\kappa \simeq 2M$

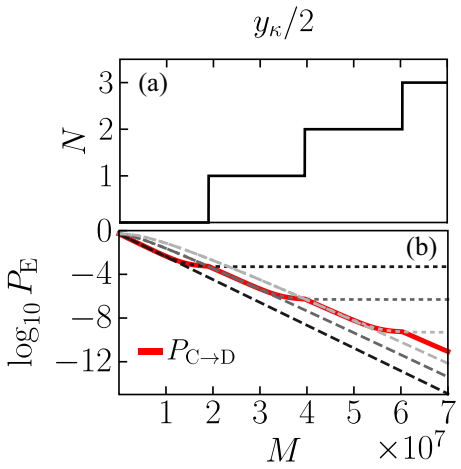

FIG. 3. (a) Optimal decision threshold of the photon counts N. (b) Error probability vs the number of copies M with $N_S = 0.001$, $N_E = 20$, and $\kappa = 0.01$. The abrupt changes of $P_{C\to D}$ happen when the optimal decision threshold changes in (a). The dashed lines from dark to light represent the error probabilities corresponding to the decision threshold $N = 0, 1, 2$, respectively, according to the approximation in Eq. (30). The dotted lines from dark to light indicate the exact error probabilities for the same thresholds calculated with Eq. (29).

to obtain the leading-order results. Then, we arrive at the analytical result

$$P_{C\to D} \approx P_H[\hat{\rho}_{0,N_S}, \hat{\rho}_{1,\kappa}(\sigma_\kappa\sqrt{2M})] \tag{27}$$

$$= \left[1 - \sum_{n:\gamma_{n,\kappa}(2M)>0} \gamma_{n,\kappa}(2M)\right] \Big/ 2. \tag{28}$$

We numerically verified that the above expression agrees with the exact result with negligible error in all the parameter regions relevant to this paper (see Appendix C).

In Fig. 3(b), we plot QI performance $P_{C\to D}$ as the red curve for the same parameter choice of Refs. [5,27]. We see abrupt changes in the error probability when the number of modes M increases, due to the integer summation in Eq. (28). To better understand the performance, we consider a threshold decision strategy, where one compares the measured photon number against a threshold N: target presence is declared if and only if the photon number is larger than N. From Eq. (28), the error probability of such a threshold decision is

$$P^N_{C\to D} = \frac{1}{2}\left[1 - \sum_{n=0}^{N} \gamma_{n,\kappa}(2M)\right]. \tag{29}$$

We plot $P^N_{C\to D}$ as the dotted lines for different values of N and they agree with $P_{C\to D}$ within each continuous sector (solid red curve). The abrupt change of $P_{C\to D}$ also corresponds well with the change in the optimal decision threshold $\mathrm{argmin}_N P^N_{C\to D}$ in Fig. 3(a).

After understanding the performance enabled by the conversion module, now we compare the QI error probability $P_{C\to D}$ of Eq. (28) with that of CI to show the entanglement's advantage. In CI with coherent-state probes, due to the uniform random-phase noise, the received state is photon number diagonal, and the Helstrom limit can be efficiently evaluated (see Appendix B). As Fig. 3 already has too many lines, we reprint $P_{C\to D}$ (red solid) in Fig. 4(a) in comparison with the error probability of CI (black solid) and showing orders-of-magnitude advantage. In particular, the curves indicate that QI and CI still have different error exponents despite the fully random phase noise, as we will confirm in the next section with asymptotic analyses.

B. Asymptotic results and error exponent

To better understand the QI performances, and in particular to understand the error exponent in the presence of the random-phase noise, we explore asymptotic solutions of $P_{C\to D}$. Considering Eqs. (27) and (18) at the low brightness ($N_S \ll 1$) and low reflectivity ($\kappa \ll 1$) limit, we can approximate the noisy displaced thermal state in Eq. (18) as a coherent state and $\hat{\rho}_{0,N_S}$ as a vacuum state. Therefore, Eq. (25) can be approximated as $\gamma_{n,\kappa}(y_\kappa) = \delta_{n,0} - e^{-\xi_\kappa y_\kappa}(\xi_\kappa y_\kappa)^n/n!$, where $\delta_{n,0}$ is the Kronecker delta function.

Given a threshold N, from Eq. (29), the error probability of the C→D conversion module in the large-M limit is

$$P^N_{C\to D} \approx \frac{1}{2}\sum_{n=0}^{N} p_n, \quad \text{with} \quad p_n = e^{-2\xi_\kappa M}(2\xi M)^n/n! \tag{30}$$

and the minimum error probability $P_{C\to D} = \min_N P^N_{C\to D}$. When the photon number threshold $N = 0$, it is just the error probability of the Kennedy receiver and $P^0_{C\to D} = (1/2)e^{-2\xi_\kappa M}$ [33]. The dashed lines in Fig. 3(b) show the approximated error probabilities for the decision threshold $N = 0, 1, 2$, respectively. We see a good recovery of the $P_{C\to D}$ (solid red curve) in each continuous sector, which allows us to proceed with the asymptotic analyses.

Next, we obtain the asymptotic optimal decision threshold. Considering Eq. (27), now we treat $\hat{\rho}_{0,N_S}$ as the thermal state again. Its density matrix is diagonal, with elements $p'_n = N_S^n/(1+N_S)^{n+1}$. The optimal threshold is determined by solving $p_N = p'_N$, where p_N is defined in Eq. (30), and we obtain

$$N \approx \frac{2\xi_\kappa M}{\epsilon}, \tag{31}$$

where $\epsilon = -W_{-1}(-N_S/e) \gg 1$ and W_{-1} is the Lambert W function. The approximation holds when $M \gg 1$. An asymptote of the Helstrom limit $P^{ASY}_{C\to D}$ can be obtained by substituting Eq. (31) into Eq. (30) and its error exponent can be obtained as (see Appendix D)

$$r^{ASY}_{C\to D} = \lim_{M\to\infty} \tilde{r}^{ASY}_{C\to D}(M) = [1 - \ln(e\epsilon)/\epsilon]2\xi_\kappa, \tag{32}$$

where we defined the finite-M exponent:

$$\tilde{r}^{ASY}_{C\to D} \equiv -\ln P^{ASY}_{C\to D}(M)/M. \tag{33}$$

Now we evaluate $P^{ASY}_{C\to D}$ in Fig. 4(a) as the black dashed curve. Indeed, we see a good agreement with $P_{C\to D}$ of Eq. (28)

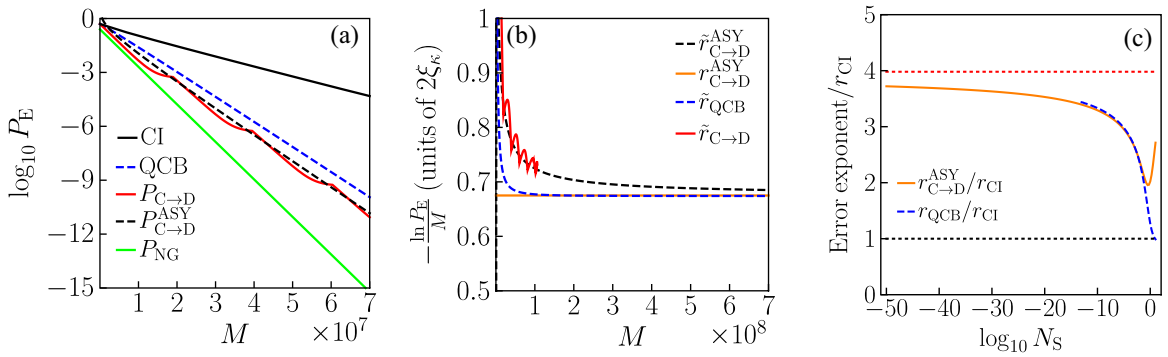

FIG. 4. The error performance for the uniform phase and known reflectivity model with the parameters $N_S = 0.001$, $N_E = 20$, and $\kappa = 0.01$. Note: some lines are only partially plotted in a range of x axis limited by numerical precision. (a) The error probabilities and bounds thereof as a function of M. The red line indicates the error probability limit of the C→D conversion. The black dashed line is the asymptote of this probability. The blue and green lines are the QCB (upper bound) and NG lower bound, respectively. The black line indicates the optimum CI's error probability. (b) The asymptotic behaviors of $-\ln P_E/M$ (whose asymptotic limits are the error exponents) with P_E being the error performance of the C→D conversion module (red), the asymptote (black, dashed), and the QCB (blue, dashed), respectively. The orange line indicates the error exponent of the asymptote. (c) The error exponent (normalized by the error exponent of the CI) of the asymptote and QCB. When $N_S \to 1^-$, the error exponent of the asymptote deviates from QCB and the low brightness condition does not hold anymore. The red dotted line indicates the 6-dB advantage over CI.

(red solid). To understand the error exponent, we plot the error probability in a logarithmic version $-\ln P_E/M$ in units of $2\xi_\kappa$ [see Eq. (26)] versus the number of modes M in Fig. 4(b). As expected, $\tilde{r}^{ASY}_{C\to D}$ (black dashed) approaches $r^{ASY}_{C\to D}$ (orange solid) in the large-M limit. The exact result $P_{C\to D}$ (red solid) agrees well with $\tilde{r}^{ASY}_{C\to D}$; however, its evaluation is limited to rather small M due to numerical precision constraints. The oscillation in the small-M region is due to the integer effect of the decision threshold, as we can see in Fig. 4(a). Due to the ratio over M, the oscillation there becomes visually more significant in Fig. 4(b).

With the error exponent $r^{ASY}_{C\to D}$ in hand, we can now compare with the error exponent of CI $r_{CI} = \lim_{M\to\infty} -\ln(P_{CI})/M$ (see Appendix B for the calculation of P_{CI}) to understand the quantum advantage in the error exponent under different signal brightness. As shown in Fig. 4(c), $r^{ASY}_{C\to D}$ (orange solid) is always larger than r_{CI}, confirming quantum advantage; moreover, the error exponent ratio approaches 6 dB (indicated by the red dotted line) as N_S approaches zero, although the rate of convergence is very slow. This can be confirmed analytically from Eq. (32) via

$$\lim_{N_S\to 0} r^{ASY}_{C\to D} = 2\xi_\kappa \simeq \kappa N_S/N_E. \tag{34}$$

As we have $r_{CI} \lesssim \kappa N_S/4N_E$, there is indeed a 6-dB advantage of QI over CI. From the numerical results as well as asymptotic analyses, we see that in the weak signal limit phase noise essentially does not change the error exponent, compared to the case without phase noise [4,27].

C. Upper and lower bounds

Finally, we provide additional comparison of the QI performance with upper and lower bounds. We obtain the upper bound from the asymptotically tight QCB [21,24] and the lower bound from the Nair-Gu (NG) bound [23].

Given any two quantum states $\hat{\rho}_0$ and $\hat{\rho}_1$, the QCB $P_{QCB}(\hat{\rho}_0, \hat{\rho}_1) = (1/2)\inf_{s\in[0,1]} Q_s$, where $Q_s = \mathrm{Tr}(\hat{\rho}_0^s \hat{\rho}_1^{1-s})$, is an asymptotically tight upper bound for the Helstrom limit $P_H[\hat{\rho}_0, \hat{\rho}_1]$. Therefore, for the uniform phase and known reflectivity model, we can apply the QCB on the Helstrom limit $P_H[\hat{\rho}_{0,N_S}, \hat{\rho}_{I,\kappa}(\sigma_\kappa\sqrt{y_\kappa})]$ in Eq. (27) to obtain the upper bound:

$$P_{C\to D} \leqslant P_{QCB,U} \equiv \frac{\inf_{s\in[0,1]} \mathrm{Tr}\left[\hat{\rho}^s_{0,N_S} \hat{\rho}^{1-s}_{I,\kappa}(\sigma_\kappa\sqrt{2M})\right]}{2}. \tag{35}$$

Here both $\hat{\rho}_{0,N_S}$ and $\hat{\rho}_{I,\kappa}$ are diagonal in the number state basis and therefore can be efficiently evaluated.

Nair and Gu derived a lower bound P_{NG} on the error probability of QI [23] target detection assisted by an arbitrary form of entanglement. As this is the lower bound in the ideal case, it also holds as a lower bound in the presence of additional noise. Considering M probes with mean photon number N_S, we then have

$$P_{C\to D} \geqslant P_{NG} = \tfrac{1}{4} e^{-\beta M N_S}, \tag{36}$$

where $\beta = -\ln[1 - \kappa/(N_E(1-\kappa)+1)]$.

We plot the upper bound $P_{QCB,U}$ (blue dashed) and lower bound P_{NG} (green solid) in Fig. 3(a). Meanwhile, we also plot the QCB error exponent $r_{QCB} \equiv \lim_{M\to\infty} -\ln P_{QCB,U}/M$ and $\tilde{r}_{QCB} \equiv -\ln P_{QCB,U}/M$ in Figs. 3(b) and 3(c). Indeed, we see that QCB verifies our previous asymptotic evaluations.

V. PERFORMANCE FOR THE RAYLEIGH-FADING MODEL

With the performance degradation from phase noise well understood, now we consider Rayleigh-fading targets, where the target has a Rayleigh-distributed reflectivity besides a uniform random phase [26,34–37], i.e.,

$$P_K(\kappa) = e^{-\kappa/\bar{\kappa}}/\bar{\kappa}, \tag{37}$$

with $\bar{\kappa}$ being the average reflectivity of the target (see Appendix E). Note the above distribution is up to a cutoff so that $\kappa \in [0, 1]$.

As Eqs. (17) and (19) are now difficult to calculate numerically, to understand the QI performance for Rayleigh-fading targets, we consider lower bounds and achievable performance (upper bounds).

A. Lower bound

Applying concavity of the Helstrom limit (see Lemma 1 in Ref. [26]) to Eqs. (17) and (19), a low bound of the performance $P_{\mathrm{E,LB}}$ can be obtained:

$$\begin{aligned} P_{\mathrm{C}\to\mathrm{D}} &\geqslant P_{\mathrm{E,LB}} \\ &\equiv \int d^{2M}\boldsymbol{x} d\kappa P_{K,X}(\kappa,\boldsymbol{x}) P_{\mathrm{H}}[\hat{\rho}_{0,N_{\mathrm{S}}}, \hat{\rho}_{\mathrm{I},\kappa}(\boldsymbol{x})] \\ &= \int d\kappa dy_\kappa \frac{1}{\bar{\kappa}} e^{-\kappa/\bar{\kappa}} P^{(2M)}_{\chi^2}(y_\kappa) P_{\mathrm{H}}[\hat{\rho}_{0,N_{\mathrm{S}}}, \hat{\rho}_{\mathrm{I},\kappa}(\sigma_\kappa\sqrt{y_\kappa})] \\ &\approx \int d\kappa \frac{1}{\bar{\kappa}} e^{-\kappa/\bar{\kappa}} P_{\mathrm{H}}[\hat{\rho}_{0,N_{\mathrm{S}}}, \hat{\rho}_{\mathrm{I},\kappa}(\sqrt{2M}\sigma_\kappa)]. \end{aligned} \tag{38}$$

In the last step, we have taken the approximation at the $M \gg 1$ limit, similar to Eq. (27). Now Eq. (38) can be evaluated via an approach similar to Eq. (23).

B. Achievable performance

We then explore an achievable performance of the C→D conversion module for the Rayleigh-fading model. Upon the heterodyne measurement results on the return $\boldsymbol{x}$, we perform direct photon counting on the idler output in state $\hat{\rho}_{\mathrm{I}}(\boldsymbol{x})$ from the conversion module, then finish with a threshold decision strategy at a fixed threshold independent of $\boldsymbol{x}$. With the decision threshold optimized, the error probability can be expressed as

$$\begin{aligned} P_{\mathrm{C}\to\mathrm{D}} &= P_{\mathrm{H}}\left[\hat{\rho}_{0,N_{\mathrm{S}}}, \int d^{2M}\boldsymbol{x} P_X(\boldsymbol{x}) \hat{\rho}_{\mathrm{I}}(\boldsymbol{x})\right] \\ &= P_{\mathrm{H}}\left[\hat{\rho}_{0,N_{\mathrm{S}}}, \int d\kappa dy_\kappa \frac{1}{\bar{\kappa}} e^{-\kappa/\bar{\kappa}} P^{(2M)}_{\chi^2}(y_\kappa) \hat{\rho}_{\mathrm{I},\kappa}(\sigma_\kappa\sqrt{y_\kappa})\right] \\ &\approx P_{\mathrm{H}}\left[\hat{\rho}_{0,N_{\mathrm{S}}}, \int d\kappa \frac{1}{\bar{\kappa}} e^{-\kappa/\bar{\kappa}} \hat{\rho}_{\mathrm{I},\kappa}(\sqrt{2M}\sigma_\kappa)\right], \end{aligned} \tag{39}$$

where in the last step the measurement result $y_\kappa \simeq 2M$ at the large-M limit.

Figure 5 plots the achievable performance $P_{\mathrm{C}\to\mathrm{D}}$ (red solid), the lower bound $P_{\mathrm{E,LB}}$ (purple dashed), and the optimum CI's error probability (black solid, see Appendix B) versus the number of modes. We see that the quantum advantage over CI persists for the Rayleigh-fading model, although it is further reduced when compared with the random-phase model. The plot also shows that our results agree with the QI detection for the Rayleigh-fading targets with the sum-frequency generation (SFG) reception P_{SFG} [26] (blue dashed), where the error probability decays with the number of modes in a polynomial fashion. Indeed, we find the achievable result $P_{\mathrm{C}\to\mathrm{D}}$ of the conversion module agrees fairly well with P_{SFG}. While the SFG results require an approximate solution of a complex quantum nonlinear optical process, the conversion module's achievable performance is almost exact, and requires little effort in calculations.

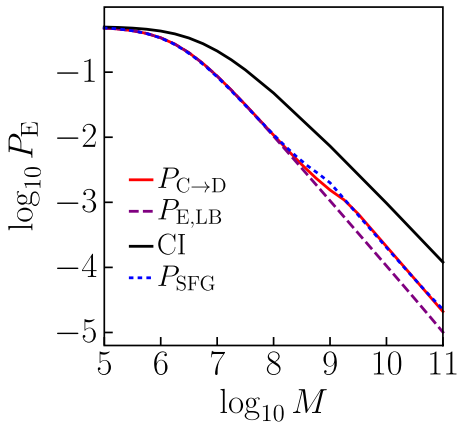

FIG. 5. The error performance for the Rayleigh-fading model. The parameters are $N_{\mathrm{S}} = 0.001$, $N_{\mathrm{E}} = 20$, and $\bar{\kappa} = 0.01$. Shown is a comparison of the achievable error performance given by Eq. (39) (red), the lower bound given by Eq. (38) (purple, dashed), the optimum error probability for CI (black), and the error performance of SFG receiver (blue, dotted).

VI. CONCLUSIONS

We study the entanglement-assisted target detection performance of the recently proposed correlation-to-displacement conversion module, in the more practical scenario of random-phase noise and reflectivity fluctuation. The results show, in the scenario of only random-phase noise, this module still affords 6-dB error exponent advantage over the optimum classical illumination when the signal brightness is small. When considering the Rayleigh reflection, the advantage is much smaller, although it is nonzero.

ACKNOWLEDGMENTS

This project is supported by NSF CAREER Grant No. CCF-2142882 and NSF Grants No. OIA-2134830 and No. OIA-2040575. Q.Z. also acknowledges support from the Defense Advanced Research Projects Agency under Young Faculty Award Grant No. N660012014029, NSF Engineering Research Center for Quantum Networks Grant No. 1941583, and Raytheon Missiles and Defense.

APPENDIX A: PROOF OF THE DIAGONAL DENSITY MATRIX OF $\hat{\rho}_{\mathrm{I}}$ UNDER UNIFORM PHASE ROTATION

Phase rotation $\hat{a} \to e^{-i\theta}\hat{a}$ on mode $\hat{a}$ is described by the unitary $\hat{R}(\theta) = \exp[-i\theta\hat{a}^\dagger\hat{a}]$. Under a uniform random phase, any single-mode input state becomes number-state diagonal, because

$$\begin{aligned} \langle m| \int d\theta\, \hat{R}(\theta)\hat{\rho}\hat{R}^\dagger(\theta)|n\rangle &= \int d\theta\, e^{-i\theta(m-n)} \langle m|\hat{\rho}|n\rangle \\ &\propto \delta_{mn}\langle n|\hat{\rho}|n\rangle, \end{aligned} \tag{A1}$$

where we utilized the fact that $\hat{R}(\theta)\,|n\rangle = e^{-in\theta}\,|n\rangle$.

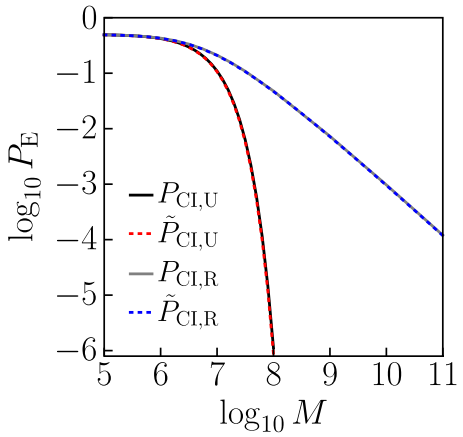

FIG. 6. Comparison of the error performances for CI evaluated by Eq. (B1) (solid) and Eq. (B3) (dotted), respectively. $P_{\mathrm{CI,U}}$ and $\tilde{P}_{\mathrm{CI,U}}$ are for the random-phase model. $P_{\mathrm{CI,R}}$ and $\tilde{P}_{\mathrm{CI,R}}$ are for the Rayleigh-fading model.

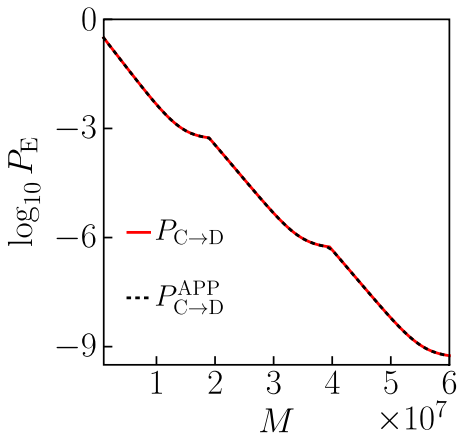

FIG. 7. Comparison of the exact (red) and approximated (black, dotted) performance limit for the random-phase model in the large-M limit.

In the case of a displaced thermal state, we have [32]

$$\begin{aligned}&\langle m|\,\hat{\rho}_{\mathrm{I},\kappa}(x)\,|n\rangle\\&=\int d\theta\frac{1}{2\pi}\,\langle m|\,\hat{\rho}_{\mu_\kappa x e^{i\theta},E_\kappa}\,|n\rangle\\&=\frac{\delta_{m,n}E^n}{(1+E)^{1+n}}e^{-|\mu_\kappa x|^2/E}\,{}_1\tilde{F}_1\left[n+1,1,\frac{|\mu_\kappa x|^2}{E(1+E)}\right].\end{aligned}\tag{A2}$$

APPENDIX B: OPTIMUM PERFORMANCE LIMIT OF CLASSICAL ILLUMINATION

For comparison, the Helstrom limit of CI is calculated with a coherent-state transmitter. If κ and θ are fixed, the return mode is in a displaced thermal state $\hat{\rho}_{\sqrt{\kappa N_S},(1-\kappa)N_E}$. When κ and θ are random variables, the output state is then $\int d\theta d\kappa P_\Theta(\theta)P_K(\kappa)\hat{\rho}_{\sqrt{\kappa N_S},(1-\kappa)N_E}$. Therefore, the performance limit is

$$P_{\mathrm{CI}}=\frac{1}{2}\left(1-\sum_{n:\gamma_{n,\mathrm{CI}}>0}\gamma_{n,\mathrm{CI}}\right),\tag{B1}$$

where the summation $\sum$ includes all the positive values of

$$\begin{aligned}\gamma_{n,\mathrm{CI}}=&\frac{N_E^n}{(1+N_E)^{n+1}}-\int d\kappa P_K(\kappa)\frac{E'^n}{(1+E')^{1+n}}\\&\times e^{-M\kappa N_\mathrm{S}/E'}\,{}_1\tilde{F}_1\left[n+1,1,\frac{M\kappa N_\mathrm{S}}{E'(1+E')}\right].\end{aligned}\tag{B2}$$

Here $E'=(1-\kappa)N_E$.

To double check the result, we calculate the performance limit with another method [26]

$$P_{\mathrm{CI}}=\min_{P_\mathrm{F}^{\mathrm{CI}}}\left[P_\mathrm{F}^{\mathrm{CI}}/2+\left(1-P_\mathrm{D}^{\mathrm{CI}}\right)/2\right]\tag{B3}$$

and compare the results. Here the conditional false-alarm probability $P_\mathrm{F}^{\mathrm{CI}}$ denotes the chance that the target presence is declared when no target is present, and the conditional detection probability $P_\mathrm{D}^{\mathrm{CI}}$ denotes the chance that the target presence is declared when a target is present. The relation between $P_\mathrm{F}^{\mathrm{CI}}$ and $P_\mathrm{D}^{\mathrm{CI}}$ is referred to as the receiver operating characteristic (ROC). The ROC for the CI detection of the uniform-phase and known-reflectivity targets is $P_\mathrm{D}^{\mathrm{CI}}=Q(\sqrt{2\kappa MN_S/E'},\sqrt{-2\ln P_\mathrm{F}^{\mathrm{CI}}})$, where $Q(a,b)$ is Marcum's Q function. The CI ROC for the Rayleigh-fading targets is $P_\mathrm{D}^{\mathrm{CI}}=(P_\mathrm{F}^{\mathrm{CI}})^{1/(1+M\bar{\kappa}N_\mathrm{S}/E')}$ [38]. Figure 6 shows that the results calculated with the two methods are consistent.

APPENDIX C: LARGE-M APPROXIMATION

Figure 7 shows the exact result of Eq. (23) and approximated performance limits of Eq. (28) for M in the range of 10^6 to 6×10^7. The maximal deviation for the data we have is 0.25%, which happens when $M=10^6$. This approximation is also used in the calculation of the QCB performance for the random-phase model and the error performance for the Rayleigh-fading model under the condition of large M.

APPENDIX D: ASYMPTOTE OF THE ERROR PROBABILITY FOR THE RANDOM-PHASE MODEL

Consider the scenario of uniformly distributed phase shift and a fixed known reflectivity. In the asymptotic limit of low brightness $N_\mathrm{S}\ll1$ and low reflectivity $\kappa\ll1$, the optimal decision threshold N is determined by solving

$$\frac{N_\mathrm{S}^N}{(1+N_\mathrm{S})^{N+1}}=e^{-2\xi_\kappa M}(2\xi_\kappa M)^N/N!,\tag{D1}$$

which leads to the solution

$$N\approx-W_{-1}^{-1}\left[-N_\mathrm{S}\left(\frac{1}{1+N_\mathrm{S}}\right)^{1+1/N}\frac{(2\pi N)^{1/N}}{e}\right]2\xi_\kappa M.\tag{D2}$$

In the derivation above, we have used Stirling's approximation $N!\approx\sqrt{2\pi N}(N/e)^N$. When $N\gg1$ and $N_S\ll1$, Eq. (31) is obtained by further approximation. Substituting Eq. (31) into Eq. (30), an asymptote of $P_{\mathrm{C}\to\mathrm{D}}$ is obtained:

$$\begin{aligned}P_{\mathrm{C}\to\mathrm{D}}^{\mathrm{ASY}}&\approx\frac{1}{2}e^{-2\xi_\kappa M}(2\xi_\kappa M)^N/N!\\&\approx\frac{1}{2}e^{-2\xi_\kappa M}\frac{(2\xi_\kappa M)^N}{\sqrt{2\pi N}(N/e)^N}\\&\approx\frac{1}{2}e^{-2\xi_\kappa M}\frac{(2\xi_\kappa M)^{2\xi_\kappa M/\epsilon}}{\sqrt{4\pi\xi_\kappa M/\epsilon}(2\xi_\kappa M/\epsilon e)^{2\xi_\kappa M/\epsilon}}.\end{aligned}\tag{D3}$$

The approximation in the first line holds because $2\xi_\kappa M/N \gg 1$. The finite-M error exponent

$$\tilde{r}^{\mathrm{ASY}}_{\mathrm{C}\to\mathrm{D}}(M) = -\frac{1}{M}\ln P^{\mathrm{ASY}}_{\mathrm{C}\to\mathrm{D}} \approx \frac{1}{M}\left[\left(1-\frac{\ln e\epsilon}{\epsilon}\right)2\xi_\kappa M+\frac{1}{2}\ln 2\xi_\kappa M+\ln 2\sqrt{2\pi/\epsilon}\right]. \tag{D4}$$

APPENDIX E: RAYLEIGH DISTRIBUTION

For non-negative-valued random variable $z=\phi(\kappa)=\sqrt{\kappa}$, the probability density function (PDF) of the Rayleigh distribution is $P_{\sqrt{K}}(z)=2ze^{-z^2/\bar{\kappa}}/\bar{\kappa}$ [26,39]. As $\phi(\kappa)$ is a strictly monotonic, differentiable function, the PDF of κ can be obtained by using the change-of-variable technique (see Theorem 7.1 in Ref. [40]):

$$P_K(\kappa)=P_{\sqrt{K}}(\phi(\kappa))\times|\phi'(\kappa)|=e^{-\kappa/\bar{\kappa}}/\bar{\kappa}. \tag{E1}$$

[1] B. M. Escher, R. L. de Matos Filho, and L. Davidovich, General framework for estimating the ultimate precision limit in noisy quantum-enhanced metrology, Nat. Phys. **7**, 406 (2011).

[2] C. N. Gagatsos, B. A. Bash, S. Guha, and A. Datta, Bounding the quantum limits of precision for phase estimation with loss and thermal noise, Phys. Rev. A **96**, 062306 (2017).

[3] S. Lloyd, Enhanced sensitivity of photodetection via quantum illumination, Science **321**, 1463 (2008).

[4] S.-H. Tan, B. I. Erkmen, V. Giovannetti, S. Guha, S. Lloyd, L. Maccone, S. Pirandola, and J. H. Shapiro, Quantum Illumination with Gaussian States, Phys. Rev. Lett. **101**, 253601 (2008).

[5] Q. Zhuang, Z. Zhang, and J. H. Shapiro, Optimum Mixed-State Discrimination for Noisy Entanglement-Enhanced Sensing, Phys. Rev. Lett. **118**, 040801 (2017).

[6] Q. Zhuang, Quantum Ranging with Gaussian Entanglement, Phys. Rev. Lett. **126**, 240501 (2021).

[7] Q. Zhuang and J. H. Shapiro, Ultimate Accuracy Limit of Quantum Pulse-Compression Ranging, Phys. Rev. Lett. **128**, 010501 (2022).

[8] M. Sarovar and G. Milburn, Optimal estimation of one-parameter quantum channels, J. Phys. A: Math. Gen. **39**, 8487 (2006).

[9] H. Venzl and M. Freyberger, Quantum estimation of a damping constant, Phys. Rev. A **75**, 042322 (2007).

[10] A. Monras and M. G. A. Paris, Optimal Quantum Estimation of Loss in Bosonic Channels, Phys. Rev. Lett. **98**, 160401 (2007).

[11] G. Adesso, F. Dell'Anno, S. De Siena, F. Illuminati, and L. A. M. Souza, Optimal estimation of losses at the ultimate quantum limit with non-Gaussian states, Phys. Rev. A **79**, 040305(R) (2009).

[12] A. Monras and F. Illuminati, Information geometry of gaussian channels, Phys. Rev. A **81**, 062326 (2010).

[13] A. Monras and F. Illuminati, Measurement of damping and temperature: Precision bounds in gaussian dissipative channels, Phys. Rev. A **83**, 012315 (2011).

[14] R. Nair, Discriminating quantum-optical beam-splitter channels with number-diagonal signal states: Applications to quantum reading and target detection, Phys. Rev. A **84**, 032312 (2011).

[15] R. Nair and M. Tsang, Far-Field Superresolution of Thermal Electromagnetic Sources at the Quantum Limit, Phys. Rev. Lett. **117**, 190801 (2016).

[16] R. Nair, Quantum-Limited Loss Sensing: Multiparameter Estimation and Bures Distance between Loss Channels, Phys. Rev. Lett. **121**, 230801 (2018).

[17] S. Pirandola and C. Lupo, Ultimate Precision of Adaptive Noise Estimation, Phys. Rev. Lett. **118**, 100502 (2017).

[18] H. Shi and Q. Zhuang, Ultimate precision limit of noise sensing and dark matter search, npj Quantum Inf. **9**, 27 (2023).

[19] R. Nair, G. Y. Tham, and M. Gu, Optimal Gain Sensing of Quantum-Limited Phase-Insensitive Amplifiers, Phys. Rev. Lett. **128**, 180506 (2022).

[20] C. Weedbrook, S. Pirandola, R. García-Patrón, N. J. Cerf, T. C. Ralph, J. H. Shapiro, and S. Lloyd, Gaussian quantum information, Rev. Mod. Phys. **84**, 621 (2012).

[21] S. Pirandola and S. Lloyd, Computable bounds for the discrimination of Gaussian states, Phys. Rev. A **78**, 012331 (2008).

[22] L. Banchi, Q. Zhuang, and S. Pirandola, Quantum-Enhanced Barcode Decoding and Pattern Recognition, Phys. Rev. Appl. **14**, 064026 (2020).

[23] R. Nair and M. Gu, Fundamental limits of quantum illumination, Optica **7**, 771 (2020).

[24] K. M. R. Audenaert, J. Calsamiglia, R. Muñoz-Tapia, E. Bagan, L. Masanes, A. Acin, and F. Verstraete, Discriminating States: The Quantum Chernoff Bound, Phys. Rev. Lett. **98**, 160501 (2007).

[25] S. Guha and B. I. Erkmen, Gaussian-state quantum-illumination receivers for target detection, Phys. Rev. A **80**, 052310 (2009).

[26] Q. Zhuang, Z. Zhang, and J. H. Shapiro, Quantum illumination for enhanced detection of Rayleigh-fading targets, Phys. Rev. A **96**, 020302(R) (2017).

[27] H. Shi, B. Zhang, and Q. Zhuang, Fulfilling entanglement's benefit via converting correlation to coherence, arXiv:2207.06609 (2022).

[28] Q. Zhuang, Quantum-Enabled Communication without a Phase Reference, Phys. Rev. Lett. **126**, 060502 (2021).

[29] C. Helstrom, Quantum detection and estimation theory, J. Stat. Phys. **1**, 231 (1969).

[30] C. Helstrom, *Quantum Detection and Estimation Theory* (Academic Press, New york, 1976).

[31] C. Helstrom, Minimum mean-squared error of estimates in quantum statistics, Phys. Lett. A **25**, 101 (1967).

[32] H. Shi, Z. Zhang, and Q. Zhuang, Practical Route to Entanglement-Assisted Communication Over Noisy Bosonic Channels, Phys. Rev. Appl. **13**, 034029 (2020).

[33] R. S. Kennedy, Research Laboratory of Electronics, MIT, Quarterly Progress Report **108**, 219 (1973).

[34] J. W. Goodman, Some effects of target-induced scintillation on optical radar performance, Proc. IEEE **53**, 1688 (1965).

[35] J. W. Goodman, Some fundamental properties of speckle, J. Opt. Soc. Am. **66**, 1145 (1976).

[36] J. H. Shapiro, Target-reflectivity theory for coherent laser radars, Appl. Opt. **21**, 3398 (1982).

[37] J. H. Shapiro, B. A. Capron, and R. C. Shapiro, Imaging and target detection with a heterodyne-reception optical radar, Appl. Opt. **20**, 3292 (1981).

[38] H. L. VanTrees, *Detection, Estimation, and Modulation Theory, Part I: Detection, Estimation, and Linear Modulation Theory* (John Wiley & Sons, New York, 2004), Sec. 4.4.

[39] P. Massoud Salehi, and J. Proakis, *Digital Communications* (McGraw-Hill, New York, 2008), Sec. 2.3.

[40] S. Ross, *A First Course in Probability* (Pearson, New Jersey, 2010).